Surfaces and Interfaces 94 (2026) 109468

Contents lists available at ScienceDirect

Surfaces and Interfaces

journal homepage: www.sciencedirect.com/journal/surfaces-and-interfaces

O-vacancy driven structural tuning and enhanced polaron transport in metal/amorphous MoO_3 interfaces

B. Gianfelici [a], F. Paparoni [b,a], N. Pinto [a,c,*], M. Minicucci [a], R. Gunnella [a], S.J. Rezvani [a]

[a] Physics division, School of Science and Technology, University of Camerino, via Madonna delle Carceri 9B, 62032 Camerino, Italy
[b] Synchrotron SOLEIL, L'Orme des Merisiers, Saint-Aubin, 91190 Gif-sur-Yvette, France
[c] Advanced Materials Metrology and Life Science Division, Istituto Nazionale di Ricerca Metrologica (INRiM), Strade delle Cacce 91, 10135 Torino, Italy

ARTICLE INFO

Keywords:
Amorphous-MoO_3
Metal interface
Polarons
XAS
O vacancies

ABSTRACT

In this study, we investigate metal–interface-driven O-vacancy formation within the amorphous molybdenum trioxide (a-MoO_3) lattice, in multilayer heterostructures comprising alternating metal (Au or Ti) and a-MoO_3 thin films. X-ray and Raman spectroscopies reveal a preferential depletion of O_1 sites, leading to a Mo^{5+} concentration that scales with the metal reactivity. Combining structural and electronic transport analyses, we demonstrate the tunability of the polaronic hopping mechanism via O-vacancies, as well as their role in local structural distortions and consequent modulation of bonding stiffness. Our results establish multi-metal/oxide interface architectures as effective catalysts for oxygen-vacancy engineering in amorphous oxides, enabling tunable electronic functionality in disordered systems.

1. Introduction

MoO_3 has been extensively investigated for several advanced applications ranging from electronic devices and sensors to energy storage [1–4] due to its high work function (6.7 eV) and optical band gap (3.6 eV). Most applications relied on the crystalline α-MoO_3 polymorph, due to its orthorhombic crystalline matrix characterized by distorted MoO_6 octahedra arranged in a layered structure, weakly bound by van der Waals interactions. Each octahedra is constituted by three non-equivalent oxygen sites: An apical oxygen allocated within the MoO_6 interlayer regions (O_1), two corner-sharing (O_2) and three edge-sharing (O_3) sites that connect the octahedra along the $a-c$ crystallographic plane (see Fig. 1). The control of oxygen vacancies (O_V) within the crystalline MoO_3 lattice has led to significant improvements in the material's performance across a wide range of advanced applications, including green hydrogen production [5] and energy storage [6]. Moreover, the O_V acts as n-type doping, modifying the electrical conduction of the material via creation of self-doping states that push Fermi's level toward the conduction band [7]. Recent works suggest that the final electronic structure not only depends on the vacancy concentration, but also on the defect distribution within the distinct oxygen sites [8,9].

On the other hand, compared to the well-documented crystalline MoO_3 [10], the control over the defect distribution in amorphous MoO_3 (a-MoO_3) structures remains less comprehensively addressed. Yet, even if the lack of long-range order in amorphous materials complicates defect studies compared to its crystalline counterpart, a-MoO_3 has shown superior performance in terms of electrochemical cycling [11], photothermal conversion [12], or photocatalytic activity [13] due to its thermal resistance and isotropic optical properties. Optimizing device performance also requires deep knowledge and control of the charge-transport properties in the metal oxide, which depend directly on the oxygen stoichiometry [14]. O defects in metal oxides modulate the material conductivity by donating electrons to the conduction band, forming either delocalized free electrons or polarons. Additionally, local structure distortions induced by O_V can also play a major role on the charge migration mechanism [15–18].

In the case of a-MoO_3 a polaron-hopping charge transport was recently demonstrated [19], as a consequence of an ionic imbalance within the lattice matrix of the insulating material. However, the role of polarons in the conduction process and its evolution at different defects concentration is not yet largely explored. Among the available options to carry out defect engineering, thermal treatments can be intricate, since can lead to side-product formation or metastable vacant sites [8,20]. On the other hand, the ionic redistribution within the a-MoO_3 lattice can be stably modified in the presence of metal/MoO_3 interfaces, which drives O_V formation near the interface region, as

* Corresponding author at: Physics division, School of Science and Technology, University of Camerino, via Madonna delle Carceri 9B, 62032 Camerino, Italy.
E-mail addresses: francesco.paparoni@unicam.it (F. Paparoni), nicola.pinto@unicam.it (N. Pinto).

https://doi.org/10.1016/j.surfin.2026.109468
Received 23 December 2025; Received in revised form 15 April 2026; Accepted 29 April 2026
Available online 2 May 2026

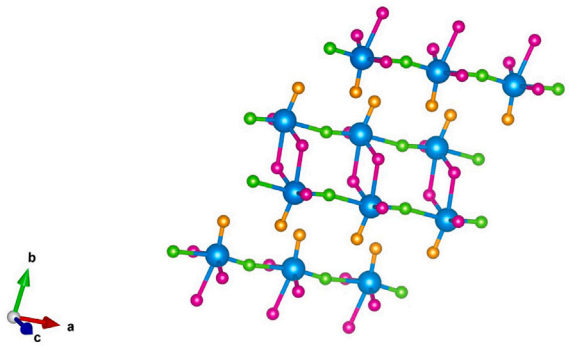

Fig. 1. α-MoO_3 structure. ● = Mo, ● = O_1, ● = O_2 and ● = O_3.

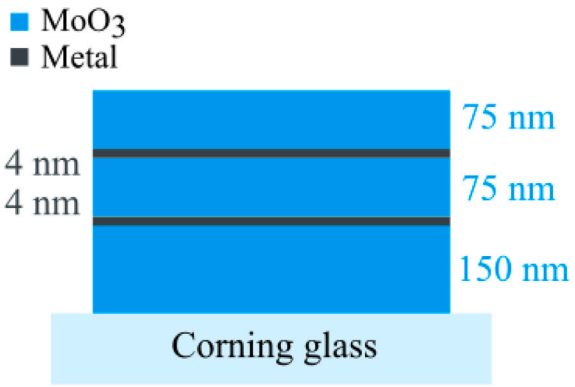

Fig. 2. Schematic drawing of the investigated multilayer structures. Metal layers used are Au or Ti.

a consequence of chemical potentials and oxidation enthalpies mismatch [8,21–27]. The resulting defect concentration and propagation are influenced by the metal's reactivity with the oxide matrix. A nanostructuring approach that creates multiple interfaces can also be expected to further enhance bulk propagation of these defects. Similar interface-engineering strategies on a-MoO_3 were used to mitigate recombination losses in hole-selective heterojunctions [14], thereby improving photocatalytic conversion efficiencies.

In this work, we have fabricated multilayer a-MoO_3/*M* thin film heterostructures using alternating RF/DC sputtering. The presence of multiple ultra-thin metallic interfaces resulted in an enhancement and greater uniformity of oxygen depletion within the metal oxide layers. Different concentrations of O_V defects were formed using metal interfaces with low (Au) or high (Ti) oxidation reactivity. Heterostructured samples were compared with a single-layer a-MoO_3 film. The defect distribution, local structural reconfiguration and resulting modulation of the conduction mechanisms within a-MoO_3 are investigated by combining structural and transport properties.

2. Methods

Samples consist of three layers of MoO_3 films and two thin metal layers (either Au or Ti) as schematized in Fig. 2, deposited both on pristine Corning glass substrates (Fig. 2) and interdigitated Corning glass substrates patterned with gold contacts to allow electrical measurements, as detailed in another work [19]. The substrate features two individually addressable linear microelectrode arrays arranged in an interdigitated configuration. Interdigitated area is about 3.5 mm. A single-layer of 300 nm thick MoO_3 film was also prepared. MoO_3 layers were deposited via radio-frequency (RF) sputtering using a MoO_3 target (99.9% purity) on a Cu backplate. Metal layers were deposited by direct current (DC) sputtering, using 99.99% pure Au and Ti metallic disk targets. A constant deposition rate of 0.3 Å s^{-1} was maintained in all cases. Both processes were conducted during the same run, maintaining an Ar partial pressure of 0.002 mbar over a base pressure of 10^{-5} mbar, while rotating the substrate holder to ensure uniform deposition. The thickness of the deposited films was monitored utilizing a quartz crystal microbalance calibrated for the density and Z-ratio of the deposited material. To ensure consistent achievement of relative layer thicknesses, tooling factors for both RF and DC sputtering sources were also accounted for, calibrating the actual thickness of a Ti film and a MoO_3 film *via* Atomic force microscopy (AFM) measurements of film edge profiles.

Prior to deposition, Corning glass substrates underwent a cleaning consisting of 15 min of sonication in acetone, followed by rinsing in deionized water and drying under N_2 flow. Interdigitated Corning glass substrates were cleaned by sequential rinsing in ethanol and deionized water, then dried under N_2 flow.

Micro-Raman spectroscopy measurements were performed using an excitation wavelength of λ = 532 nm, a 1800 ll/mm grating and a 50× magnification long-distance optic. Laser power on the sample was kept below 3 mW to avoid possible laser-induced crystallization. X-ray photoelectron spectroscopy (XPS) was conducted using an Al K_α radiation source, with a base pressure of 2×10^{-8} mbar and a pass energy of 10 eV. Spectral calibration was performed aligning the C *1s* relative to the adventitious carbon to 284.8 eV. Mo *3d* spectra were fitted according to the procedure described in a previous work [20], deconvoluting it into four components ascribable to the Mo^{6+} ($Mo_{3/2}$ 232.7 ± 0.1 eV and $Mo_{1/2}$ 235.9 ± 0.1 eV, with fixed FWHM of 1.49 and 1.56) and Mo^{5+} (231.8 ± 0.1 eV and 234.95 ± 0.1 eV, with FWHM of 1.47 and 1.6). The intensity ratio between $d_{5/2}$ and $d_{3/2}$ components was fixed to 0.67 in agreement with the degeneracy of the spin–orbit splitting. X-ray absorption spectroscopy (XAS) data were collected at the SAMBA beamline (SOLEIL synchrotron) in fluorescence mode. Spectra were normalized to the incident photon flux and calibrated with a reference Mo foil. Data analysis was carried out with FASTOSH and GNXAS packages [28,29]. Scanning electron microscopy (SEM) images were collected using "ZEISS SIGMA 300 FESEM", with a maximum resolution of 1.2 nm at 15 kV.

Electrical measurements were performed by cooling the samples in a closed-cycle He cryostat. DC resistance was measured using either an electrometer (Keithley model 6517B) or a source measure unit (Keysight model B2912A). Thin gold wires (25 μm diameter) were electrically connected to the interdigitated circuit pads on the substrate using a thin layer of carbon paste. Due to the high resistance values detected in the MoO_3 films, a two-contact measurement configuration was used.

3. Results

The homogeneity of both metal and metal oxide layers was studied by collecting energy-dispersive spectroscopy (EDX) maps. As shown in Fig. 3, our maps highlight a uniform distribution of both molybdenum and the secondary metal (Au or Ti) content throughout the samples, resulting in a granular morphology with grains ranging in diameter from 40 nm to 50 nm. No clear elemental impurities were detected, as also confirmed via XPS wide scan (see Supporting information, S1).

The role of the distinct metal interfaces formation on the a-MoO_3 surface stoichiometry was studied via XPS, fitting high-resolution Mo 3*d* spectra as shown in Fig. 4. Fitting routine of the Mo $3d_{5/2}$ and $3d_{3/2}$ doublet was carried out in agreement with previous works, as detailed in the methods section. All spectra were deconvoluted using two doublet components relative to Mo^{6+} (centered around 232.6 eV and 235.7 eV) and Mo^{5+} (centered around 231.6 eV and 234.7

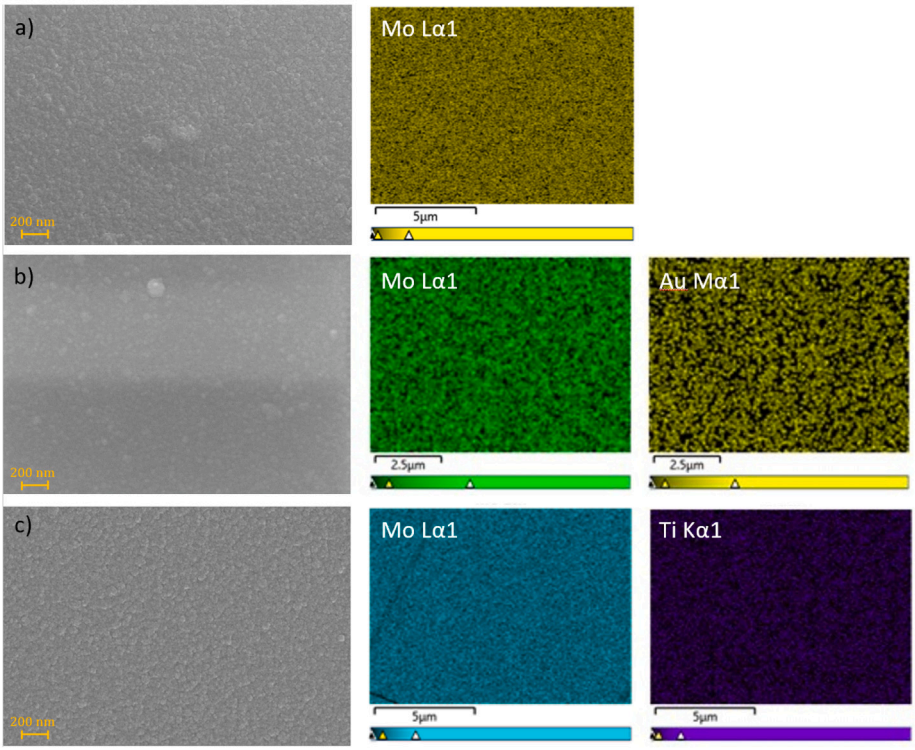

Fig. 3. SEM images (left column) of the investigated samples and elemental maps derived by EDX for Mo (center column) and for Au and Ti (right column). (a) Reference film of MoO_3, 300 nm thick; (b) MoO_3/Au; (c) MoO_3/Ti.

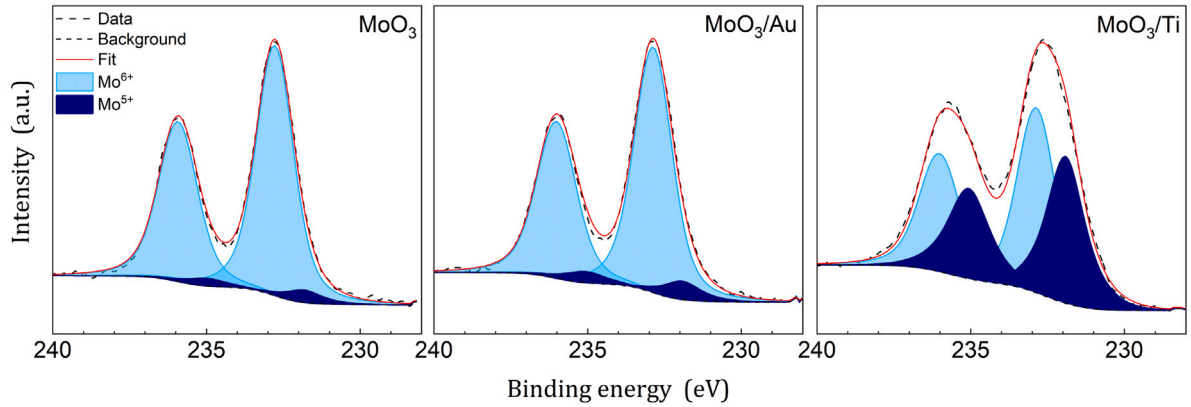

Fig. 4. XPS spectra of Mo 3*d* for the single layer of a-MoO_3 (left) and for the heterostructures of MoO_3/Au (center) and of MoO_3/Ti (right). Experimental data and least squares fits are shown as dashed and continuous lines, respectively. Mo^{6+} and Mo^{5+} contributions are reproduced as light and dark blue areas, respectively.

eV) [30,31]. No lower valent states such as Mo^{4+} or metallic Mo were detected.

The pristine MoO_3 film shows a near stoichiometric structure, as indicated by the domination of Mo^{6+} species (95.2%). On the other hand, the Mo^{5+} concentration increases to 7% in MoO_3/Au, and becomes extremely high (44%) in the MoO_3/Ti sample. These results indicate a higher defect concentration in the heterostructure than in the single-layer a-MoO_3 film, suggesting enhanced reactivity of the Ti at the MoO_3/Ti interface. The presence of defective Mo^{5+} states can be related to O_V formation as a consequence of the oxygen scavenging effect previously reported for metal/MoO_3 interfaces [25,26]. To exclude significant metal-ion penetration within the MoO_3 layers, we performed XPS and EDX analysis. The XPS wide-scan spectra did not reveal the presence of Au or Ti elements on the sample surfaces (see SI, Figure S1). EDX analysis was performed at different electron beam energies on 200 nm MoO_3 layers on 100 nm thick Au and Ti layers. The selected energies (5–8 keV) were chosen to have increasing penetration depths in the MoO_3 layers (more details in SI, Fig. S7). Our results show no significant Ti or Au characteristic X-ray emissions at 5 keV, whereas Ti and Au are detectable at 8 keV due to the underlying metal layer contribution. Hence, it is reasonable to assume negligible diffusion of both metals into the MoO_3 matrix.

To compare the surface stoichiometry with the bulk phase formation and O_V concentration, samples were analyzed by Raman spectroscopy (see Fig. 5). All samples show broad spectroscopic features that can be deconvoluted into two bending modes around 235 and 385 cm^{-1} followed by the three asymmetric stretching modes relative to triple-coordinated oxygens (~716 cm^{-1}), double-coordinated oxygens (~860 cm^{-1}) and double bonded terminal oxygen (Mo=O_1, ~955 cm^{-1}). The broadness and well-known positions of such vibrational modes compared to the α-MoO_3 crystalline phase (see powder spectra in Fig. 5) clearly confirm the formation of amorphous MoO_3

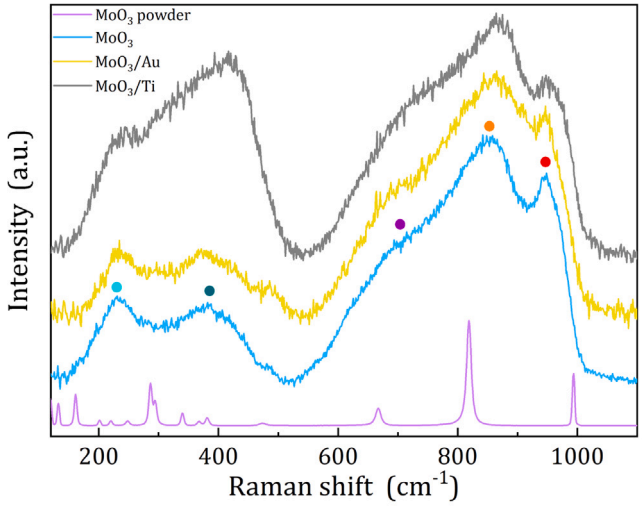

Fig. 5. Normalized Raman spectra collected from the reference film of a-MoO_3 (light blue); the MoO_3/Au (yellow) and the MoO_3/Ti (dark gray) heterostructures. Colored dots show the position of the main vibrational modes at: ● = 235 cm^{-1}, ● = 385 cm^{-1}, ● = 716 cm^{-1}, ● = 860 cm^{-1}, ● = 955 cm^{-1}. For comparison, the spectra of crystalline α-MoO_3 (pink), collected from a reference powder, is reproduced.

in all samples. Our findings are in agreement with available data on amorphous MoO_3 [19,25,32].

However, the heterostructured films evidence an increase of the relative intensity of the bending modes compared to the stretching modes. The effect is moderate in the MoO_3/Au sample while is well evident in the MoO_3/Ti case, where the bending mode at 385 cm^{-1} shifts upward around 415 cm^{-1} and its relative height increases 6 times if compared to the stretching mode around 860 cm^{-1} of a-MoO_3. As observed in other works [33,34], since a bending mode around 400 cm^{-1} can be related to Mo^{5+}-O vibrations, the modulation observed is consistent with a higher bulk concentration of Mo^{5+} ions in heterostructures, particularly in the Ti case. The presence of multiple metal interfaces enhance the defect concentration throughout the MoO_3 volume, as demonstrated by the comparison with a sample with single Ti layer (see Fig. S4 in the SI). Moreover, Fig. 5 shows a hindering and moderate blueshift of the Mo=O_1 component (red dot) in the MoO_3/Ti sample. Since the position of this feature can be directly related to the Mo–O_1 distance [35], the observation suggests an elongation of this bond.

Further insight into Mo local structural changes at distinct bulk O_V levels was obtained using XAS at the Mo K-edge. As shown in Fig. 6a, all XANES spectra evidence a pre-edge peak followed by a broad white line region. The presence of the pre-edge peak is assignable to dipole-forbidden $1s-4d$ transitions, and can be expected to appear in the presence of distorted MoO_6 octahedra, as a consequence of a more pronounced hybridization between the $5p$ and $4p$ orbitals of the Mo centers and the $2p$ orbitals of the bonded oxygens [36,37]. Our results show a modest hindering of the white line and increased pre-edge intensity when comparing the MoO_3/Au sample to the pristine a-MoO_3. This suggests that the moderately higher concentration of O_V introduced by the Au interface slightly enhances the octahedral distortion at the Mo sites, as also observed in the case of low-defective α-MoO_3 [8]. On the other hand, in the MoO_3/Ti case, we observe a hindering of the shoulder around 20 045 eV and an increase of the rest of the white line. Concurrently, the pre-edge peak intensity is reduced, suggesting the presence of more symmetric MoO_6 octahedra. Such modulations can be related to the higher concentration of Mo^{5+} in the presence of Ti interfaces, as confirmed by our linear combination fit analysis (see Figure S2) that gives a similar trend of bulk O_V concentration to the one estimated via XPS. In agreement with Raman data, XANES analysis confirms similar O_V concentrations in the samples' bulk and surface, particularly in the MoO_3/Ti case (17% ± 3%) case. The slightly higher bulk O_V concentration estimated for the MoO_3 and MoO_3/Au bulk structures (7% ± 1% and 9% ± 1%, respectively) might be attributed to either surface re-oxidation and/or vacancy-enriched regions in the proximity of the metal interface. Moreover, the linear combination fit analysis also corroborates the enhanced octahedral distortion in the MoO_3/Au case, since the best fit contains a higher concentration of references with more distorted MoO_6 octahedra.

Fourier-transformed EXAFS spectra are shown in Fig. 6b. Our results show a main scattering peak centered around 1.3 Å, which can be attributed to Mo–O_1 bonds, and a prominent shoulder near 2 Å, mainly due to Mo–O_3 bonds. The weak scattering peak observed around 3 Å can be assigned to Mo–Mo bonds, which are damped in amorphous structures due to the loss of long-range order. On the Mo–O coordination shell, we observe a significant increase of the Mo–O_3/Mo–O_1 intensity ratio between the pristine MoO_3 case and the MoO_3/Ti sample, suggesting a predominance of O_1 defects. To confirm this assertion, EXAFS spectra were fitted following the procedure described in another work [8]. Only the first O shell was fitted, using 5 two-body components related to the three non-equivalent O sites. The S_0^2 constant amplitude reduction factor was kept constant for all data. For the pristine sample data, the coordination numbers were fixed to the theoretical values while varying the Debye–Waller factors and bond lengths. The EXAFS signals from the heterostructures were then fitted, varying only the bond lengths and coordination numbers. Results are shown in Table S1 of the supporting information. Our analysis confirms a prevalence of O_1 defects in the MoO_3/Ti sample. On the other hand, all Mo–O bonds gradually elongate as the O vacancy concentration is increased, as a consequence of partial Mo center reduction upon free charge redistribution. In the MoO_3/Ti case, the elongation of the Mo–O_1 (+0.08 Å) and the shorter corner-sharing Mo–O_2 bonds (+0.17 Å) is more pronounced compared to the expansion of the longer Mo–O_3 lengths, in agreement with a symmetrization of the MoO_6 octahedra and Raman results. As shown in Figure S6, even though Mo–Mo shell fitting accuracy is limited, due to the damped long-range signal, our results do not evidence significant changes of the Mo–Mo length (~3.23 Å) or coordination numbers (2), supporting that O_V engineering mostly modulates the local MoO_6 environment with minimal change in the long-range Mo framework in the amorphous structure.

Effects related to O_V presence in the bulk of the MoO_3 lattice are not limited to the composition and structure of the material, involving also the electrical conduction processes of charge carriers, as we found in a previous work on pristine a-MoO_3 films [19]. Considering the relevance that the knowledge of the conduction mechanisms plays in device design and fabrication, we have carefully investigated the temperature dependence of the conductivity for the two kinds of heterostructures. Our findings evidence a sizeable upward shift of the conductivity curves for the two heterostructures if compared to that of the a-MoO_3 film used as a reference (see Fig. 7). In detail, at room temperature (RT), $\sigma(T)$ of the MoO_3/Au sample, increases of more than one order of magnitude, while for the MoO_3/Ti heterostructure, the rise is higher than 3 orders of magnitude. Moreover, $\sigma(T)$ curves of the two heterostructures evidence a relevant change of the slope, from 0.53 eV for the a-MoO_3 to 0.37 eV and 0.20 eV for MoO_3/Au and MoO_3/Ti, respectively.

As mentioned above and experimentally found, oxygen vacancies can form polarons in transition metal oxides [15,16,38] and their presence in crystalline MoO_3 is widely demonstrated [9,39,40] and recently also in a-MoO_3 [19]. There are two main conduction mechanisms for polarons, namely Polaronic Variable Range Hopping (PVRH) and Small Polaron Hopping (SPH). The former occurs as primary conduction mechanism below the half of the Debye temperature ($\vartheta_D/2$) while the latter occurs above $\vartheta_D/2$. In SPH, the polaron moves predominantly by thermally activated, nearest-neighbor hops among equivalent lattice sites, with a well-defined activation energy overcoming the local lattice

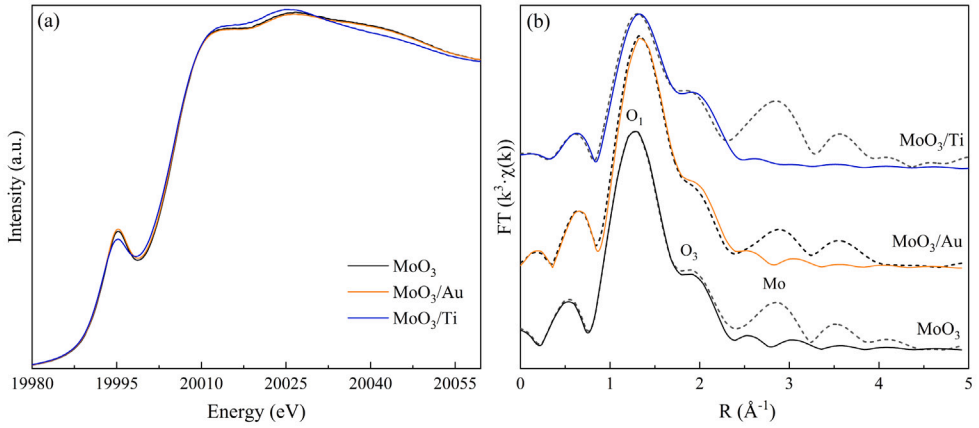

Fig. 6. (a) Mo K-edge XANES; (b) Fourier-transformed EXAFS fit (continuous lines) and experimental data (dashed lines). MoO_3/Ti FT-EXAFS is shown with an x2 multiplication factor to improve readability.

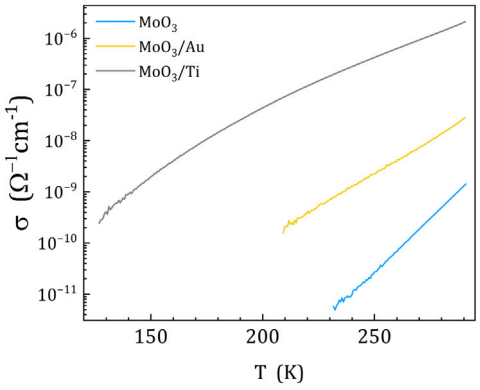

Fig. 7. Conductivity as a function of temperature of all investigated films. Noise issues have prevented detection of values below about 10^{-10} $(\Omega\ cm)^{-1}$ in MoO_3/Ti and MoO_3/Au samples.

distortion around a single site [16]. In contrast, in PVRH the polaron is still localized but can hop over different distances, choosing longer hops to more energetically favorable sites, so the hopping range and activation energy are broadly distributed rather than fixed [16].

The temperature dependence of the PVRH mechanism is expressed by the equation:

$$\sigma T^{1/2} = A exp\left[\left(-\frac{B}{T^{1/4}}\right)\right] \quad (1)$$

with:

$$B = 1.7\left(\frac{\alpha^3}{N(E_f)k_B}\right)^{1/4} \quad (2)$$

where α is the wave function decay rate, k_B is the Boltzmann constant and $N(E_F)$ the density of states close to the Fermi level.

On the other hand, for the SPH mechanism the temperature dependence is given by the following relation:

$$\sigma = \sigma_0 exp\left[\left(-\frac{W}{k_B T}\right)\right] \quad (3)$$

with W hopping energy and σ_0 a constant given by the relation

$$\sigma_0 = \left(\frac{\nu_0 N e^2 R^2}{k_B T}\right) C(1-C)e^{-2\alpha R} \quad (4)$$

where ν_0 denotes the optical phonon frequency, C the concentration of reduced ions and R the inter-ionic distance and W the activation energy.

In order to establish the prevailing conduction mechanism active in both heterostructures, $\sigma(T)$ data have been suitably replotted in Fig. 8. Our findings indicate that polarons remain the dominant transport mechanism even at the highest concentration of oxygen vacancies (Fig. 8). For the pristine a-MoO_3 film, the analysis reveals two distinct linear branches in the plotted quantities. From about 240 K up to 280 K the polaronic conduction mechanism appears to be PVRH-like (Fig. 8a). On the contrary, above 280 K the SPH mechanism prevails (Fig. 8b). Hence, $T = 280$ K represents a breakpoint for the two mechanisms. For the MoO_3/Au sample, a similar electrical behavior was detected, even if in a different T range, namely the PVRH from 225 K to about 270 K (Fig. 8a) and the SPH above 270 K (Fig. 8b). Finally, for MoO_3/Ti, the PVRH appears to be the dominant conduction mechanism up to 285 K.

Our findings suggest that the changeover temperature between the two polaronic mechanisms is modulated by the interfacial material, with a transition from 280 K for a-MoO_3 to 270 K and 285 K for MoO_3/Au and MoO_3/Ti, respectively. Based on the polaronic conduction models, the changeover T detected can be ascribed to $\vartheta_D/2$. Therefore, we can estimate a Debye temperature of 560 K, 540 K and 570 K for MoO_3, MoO_3/Au and MoO_3/Ti, respectively.

Further details on the conduction mechanism can be inferred from $N(E_F)$ and the polaron radius r_p. All results are quoted in Table 1. As can be expected, the density of states close to the Fermi level increases from about 10^{18} $(eV\ cm)^{-1}$ for the a-MoO_3 to 7.6×10^{18} for the MoO_3/Au to about 3×10^{19} for MoO_3/Ti. This fact can be related to the rise of the O_V concentration, since the extra electrons left by the O_V fill Mo *4d* orbitals, producing narrow bands within the band gap [41]. The order of magnitude of $N(E_F)$ is in agreement with results reported for other materials [42]. The r_p can be calculated using the relation [16]:

$$r_p = \frac{R}{2}\left(\frac{\pi}{6}\right)^{1/3} \quad (5)$$

with R being the distance between two possible polaron trapping sites within the same layer, which, according to previous studies [19,40], are the Mo centers. Given the short Mo–Mo distance estimated via EXAFS, (3.23 Å ±0.05 Å for all samples), Eq. (5) yields a $r_p \simeq 0.13$ nm, with a negligible difference among all the investigated samples. These findings confirm that polarons are highly localized, in agreement with a previous work on a-MoO_3 [19]. The wave function decay rate of the order of r_p^{-1} results to be about 0.77 Å^{-1}.

4. Discussion

The oxygen scavenging properties of metal interfaces in a-MoO_3 have been observed in previous works [25,26]. The interface reactivity was linked to the metal's Gibbs free energy of oxidation and to the mismatch between the metal and MoO_3 work functions (φ). In the

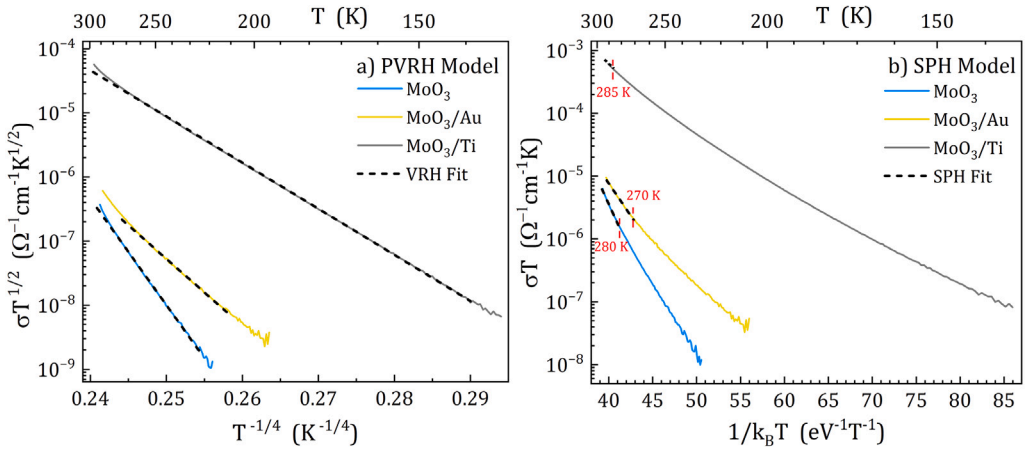

Fig. 8. Analysis of the conduction mechanisms of charge carriers in the investigated layers. PVRH (a) and SPH (b) for the reference film of MoO_3 (300 nm thick), MoO_3/Au and MoO_3/Ti. Continuous lines denote the experimental data. Dashed lines are least squares fit of data to the Eq. (1) (panel a) and Eq. (3) (panel b), respectively. Red vertical dashes show the changeover T for the polaronic conduction mechanism.

Table 1
Parameters derived from the analysis of the conductivity of all investigated samples. From left to right: Oxygen vacancy concentration estimated from XPS and XAS; resistivity at R.T.; estimated Debye temperature; density of states close to the Fermi level.

Sample	OV% (XPS)	OV% (XAS)	ρ (Ω × cm)	ϑ_D (K)	N(E_F) (eV^{-1} cm^{-3})
MoO_3	2.4 ± 0.9	7 ± 1	6.99×10^8	560	1.13×10^{18}
MoO_3/Au	3.7 ± 1.0	9 ± 1	3.56×10^7	540	7.62×10^{18}
MoO_3/Ti	22 ± 2	17 ± 3	4.74×10^5	570	3.19×10^{19}

case of a single MoO_3/Au interface, where Au oxidation is highly unfavorable, Grenier et al. [26] reported formation of Mo^{5+} species, N(Mo^{5+}), confined near the metal interface. Such a reduction results from charge transfer from the Au Fermi level to the MoO_3 conduction band. In this model, the increase of the Mo^{5+} cation has an exponential dependence with the difference in MoO_3 conduction band minimum (CB_{min} = 6.5 eV) and the metal work function (φ_{Au}= 5.2 eV [43]):

$$N(Mo^{5+}) = e^{\frac{CB_{min}-\varphi_{Au}}{k_B T}} \quad (6)$$

In our case, the moderately higher Mo^{5+} cation concentration observed in the MoO_3/Au bulk structure compared to pristine a-MoO_3 suggests a propagation of these defects. This can be attributed to facilitated ionic redistribution within the amorphous structure and to the presence of multiple metallic Au interfaces, which serve as additional vacancy-generation sites. On the other hand, the far higher effectiveness of the Ti interface compared to Au is fully consistent with this description, considering the lower φ (4.3 eV [43]) and the very negative Gibbs free energy of oxidation of Ti, which for every mole of TiO_2 formed ($1/2Ti + O \rightarrow 1/2TiO_2$ −660 kJ/mol [44]) can result in two moles of O vacancy formation in MoO_3 (+275 kJ/mol [26]). Considering that O_1 sites have the lowest-energy vacancy position in MoO_3 [9,20], the observed predominance of O_1 vacancies is thermodynamically favored compared to other non-equivalent O sites. Moreover, in agreement with our results, the formation of O_1 defects promotes the delocalization of the two electrons left in the vacant site, forming two Mo^{5+} cations for each O removal, instead of being collected at the nearest Mo site and forming a single Mo^{4+} [45].

Our analysis of the transport properties links the rise in Mo^{5+} concentration to a significant increase in the heterostructures' conductivity, while the dominant conduction mechanism is due to polarons. This behavior can be assigned to the rise of the density of states near the Fermi level, as the two e^- freed by each O_V occupy Mo *4d* defect bands and act as polaronic charge carriers. As a result, charge carriers' motion is facilitated and the polaron hopping activation energy decreases with the rise of O_V, as predicted by theoretical calculations [9].

Our findings confirm the persistence of two distinct polaronic conduction mechanisms (PVRH and SPH) in different temperature ranges, as observed in nearly-stoichiometric a-MoO_3 [19]. However, the non-monotonic evolution of the transition temperature $\vartheta_D/2$ with O_V concentration indicates a complex interplay between the lattice dynamics and defect density. Indeed, the ϑ_D trend matches the modulation of the MoO_6 distortions as demonstrated by our XANES analysis. In the low-defect regime (Au interfaces), the removal of a moderate number of O atoms breaks the local Mo–O coordination without sufficient electronic compensation, enhancing the asymmetry of the MoO_6 octahedra and softening the vibrational modes of the lattice, leading to the observed reduction in the average lattice stiffness (and then to a lowering of the Debye temperature) [38,46]. Conversely, at higher vacancy concentrations (MoO_3/Ti) we observe a mitigation of the octahedral distortions and an increase of ϑ_D. The remarkably high concentration of O_1 vacancy, estimated for MoO_3/Ti, might relate this unexpected change of ϑ_D to a phase transition towards a Mo sub-oxide, as Mo_4O_{11}, which would be thermodynamically favored for the crystalline α-MoO_3 [8,41]. However, our Raman data do not exhibit any known fingerprint of such phases, such as MoO_4 vibrations (160–180 cm^{-1} [47]). Moreover, a metallic conductivity and a value of $\vartheta_D \sim$ 400 K would have been expected in the case of Mo_4O_{11} transition [48]. These considerations suggest the persistence of the orthorhombic layered phase even at such a high level of O defects, which can be linked to the higher flexibility of the amorphous structure that can stabilize mixed valence states [49]. In this case, the hindering of lattice distortions at high O_1 defect concentration can be interpreted in terms of charge redistribution and Mo *4d* - O *2p* hybridization. The electronic structure of α-MoO_3 close to the conduction band minimum is mainly derived from the Mo *4d* orbitals [39], specifically the $4d_{xz}$, $4d_{yz}$, and $4d_{xy}$ components, while the valence band maximum originates mainly from O *2p* orbitals. This configuration produces a strong hybridization between the Mo *4d* and O *2p* states, which governs both the electronic transport properties and the local bonding within each MoO_6 octahedron. The introduction of an O_V leaves two excess electrons that localize primarily in Mo *4d* orbitals vacancy site neighboring, particularly in the $4d_{yz}$ orbital of the under-coordinated Mo and the $4d_{xz}$ orbital of a neighboring Mo atom [39]. These vacancies create extended defect states associated with two-dimensional polarons, in which the delocalized Mo 4*d* electrons interact with the O 2*p* orbitals. As the density of vacancies increases, the occupancy of Mo $4d_{xz}$ orbitals modulates the local crystal field, reducing the anisotropy in Mo–O bond lengths and angles, in agreement with our EXAFS results. This vacancy-induced symmetrization is expected

to occur particularly in the case of O_1 vacancies, as predicted by Inzani et al. [9]. Hence, the MoO_6 octahedra distortion is hindered at high O_1 vacancy concentration, resulting in an increase in the average lattice stiffness and, thus, Debye temperature.

5. Conclusions

In this work, we demonstrate that metal interface engineering in amorphous MoO_3/M multilayer films enables fine-tuning of the oxygen vacancy concentration, thereby enhancing charge carriers transport properties. The higher reactivity of the Titanium interface with the a-MoO_3 generates a remarkably high O defect concentration (44% of Mo^{5+}) compared to Au (7% of Mo^{5+}), which yields an increase of the electrical conductivity of three orders of magnitude with respect to pristine a-MoO_3. The conduction mechanisms remain governed by thermally activated polaron hopping, while the conductivity enhancement is due to an increase in the density of states near the MoO_3 Fermi level and to a substantial reduction of hopping activation energy. Analysis of structural data suggests that O_1 defect site progressively modulates the MoO_6 distortions as its concentration increases. Combining XAS analysis and conduction mechanisms, we uncover a non-monotone relation between the Debye temperature and the O_V concentration, suggesting a transition from a low-defect regime with enhanced MoO_6 distortion and lattice softening, to a high-defect regime where charge redistribution favors octahedral symmetrization and thus lattice stiffening. These findings establish multi-metal/a-MoO_3 heterostructures as a viable approach to tune electronic functionality in highly resilient materials for advanced optoelectronic or electrochemical devices. Moreover, this interface-reactivity control provides a scalable approach for tuning defect-mediated transport in a wide range of disordered oxides without high-temperature processing.

CRediT authorship contribution statement

B. Gianfelici: Writing – review & editing, Writing – original draft, Investigation, Formal analysis, Data curation. **F. Paparoni:** Writing – review & editing, Writing – original draft, Methodology, Formal analysis, Data curation, Conceptualization. **N. Pinto:** Writing – review & editing, Supervision. **M. Minicucci:** Software, Investigation. **R. Gunnella:** Resources, Writing – review & editing, Methodology. **S.J. Rezvani:** Writing – review & editing, Supervision, Funding acquisition.

Declaration of competing interest

The authors declare the following financial interests/personal relationships which may be considered as potential competing interests: S.J.Rezvani reports was provided by US air force. If there are other authors, they declare that they have no known competing financial interests or personal relationships that could have appeared to influence the work reported in this paper.

Acknowledgments

This work has been partially funded by the European Union - NextGenerationEU under the Italian Ministry of University and Research (MUR) National Innovation Ecosystem grant ECS00000041-VITALITY-Spoke 9, and is based upon work supported by the US air force office of scientific research under award numbers FA8655-23-1-7004 and FA8655-23-1-7085. We thank Synchrotron SOLEIL for provision of the beam at the SAMBA beamline through project 99250175.

Appendix A. Supplementary data

Supplementary material related to this article can be found online at https://doi.org/10.1016/j.surfin.2026.109468.

Data availability

Data will be made available on request.

References

[1] H. Ali, E.K. Shokr, Y. Taya, S.A. Elkot, M. Hasaneen, W. Mohamed, Amorphous molybdenum trioxide thin films for gas sensing applications, Sens. Act. A 335 (2022) 113355.
[2] S. Sunu, E. Prabhu, V. Jayaraman, K. Gnanasekar, T. Seshagiri, T. Gnanasekaran, Electrical conductivity and gas sensing properties of MoO_3, Sens. Act. B 101 (1) (2004) 161–174.
[3] K.A. Sankar, L. Kesavan, B. Saha, M. Jyolsnaraj, S. Mohan, P. Nandakumar, K. Mohanta, C. Kvarnström, Renewable synthesis of MoO_3 nanosheets via low temperature phase transition for supercapacitor application, Sci. Rep. 14 (2024) 25030.
[4] K. Hyung-Seok, B. Cook John, L. Hao, S. Ko Jesse, H. Tolbert Sarah, O. Vidvuds, D. Bruce, Oxygen vacancies enhance pseudocapacitive charge storage properties of MoO_{3-x}, Nat. Mat. 16 (2017) 454–460.
[5] R.S. Datta, F. Haque, M. Mohiuddin, B.J. Carey, N. Syed, A. Zavabeti, B. Zhang, H. Khan, K.J. Berean, J.Z. Ou, N. Mahmood, T. Daeneke, K. Kalantar-zadeh, Highly active two dimensional α-MoO_{3-x} for the electrocatalytic hydrogen evolution reaction, J. Mater. Chem. A 5 (2017) 24223–24231.
[6] H.-S. Kim, J.B. Cook, H. Lin, J.S. Ko, S.H. Tolbert, V. Ozolins, B. Dunn, Oxygen vacancies enhance pseudocapacitive charge storage properties of MoO_{3-x}, Nat. Mater. 16 (4) (2017) 454–460.
[7] H. Peelaers, M.L. Chabinyc, C.G. Van de Walle, Controlling n-type doping in MoO_3, Chem. Mater. 29 (6) (2017) 2563–2567.
[8] F. Paparoni, G. Tchoudinov, A. Di Cicco, E. Fonda, A. Zitolo, Z. Ebrahimpour, R. Gunnella, N. Lockwood, S. Rezvani, Unraveling oxygen vacancy formation, dynamics and site distribution in MoO_{3-x} thin films, Mat. Chem. Phys. 333 (2025) 130317.
[9] K. Inzani, T. Grande, F. Vullum-Bruer, M.S. Selbach, A Van der Waals density functional study of MoO_3 and its oxygen vacancies, J. Phys. Chem. C 120 (2016) 28959–28968.
[10] L. Lajaunie, F. Boucher, R. Dessapt, P. Moreau, Strong anisotropic influence of local-field effects on the dielectric response α-MoO_3, Phys. Rev. B 88 (11) (2013).
[11] O. Fjellvåg, A. Ruud, H. Sansteby, O. Nilsen, H. Fjellvag, Crystallization, phase stability and electrochemical performance of β-MoO_3 thin films, Cryst. Growth Des. 20, 3936–3944.
[12] C. Guo, P. Yan, C. Zhu, C. Wei, W. Liu, W. Wu, X. Wang, L. Zheng, J. Wang, Y. Du, J. Chen, Q. Xu, Amorphous MoO_{3-x} nanosheets prepared by the reduction of crystalline MoO_3 by Mo metal for LSPR and photothermal conversion, Chem. Commun. 55 (2019) 12527–12530.
[13] M. Ponce-Mosso, M. Pérez-González, P. García-Tinoco, H. Crotte-Ledesma, M. Morales-Luna, S. Tomás, Enhanced photocatalytic activity of amorphous MoO_3 thin films deposited by rf reactive magnetron sputtering, Catal. Today 349 (2020) 150–158, XXVI IIMRC (2017) Symposium F3: Advanced Catalytic Materials.
[14] D. Scirè, R. Macaluso, M. Mosca, M.P. Casaletto, O. Isabella, M. Zeman, I. Crupi, Defect density analysis of WO_x and MoO_x thin films grown by pulsed laser deposition for heterojunction solar cell applications, ACS Appl. En. Mat. 8 (13) (2025) 9016–9028.
[15] G. Greaves, Small polaron conduction in V_2O_5-P_2O_5 glasses, J. Non-Cryst. Sol. 11 (5) (1973) 427–446.
[16] M. El-Desoky, N. Gazouly, A.E. Hannor, H.A. Yousef, Adiabatic small polaron hopping conduction in nanostructured Bi_2O_3–Fe_2O_3–$PbTiO_3$ prepared by high energy planetary ball mill, J. Mat. Sci.: Mat. Elect. 34 (2023) 1234–1245.
[17] K. Takenaka, H. Komatsu, T. Sagano, K. Ide, S. Toko, T. Katase, T. Kamiya, Y. Setsuhara, Hydrogen-included plasma-assisted reactive sputtering for conductivity control of ultra-wide bandgap amorphous gallium oxide, Jap. J. Appl. Phys. 63 (4) 04SP65.
[18] F. Paparoni, E. Mijit, H. Darjazi, F. Nobili, A. Zitolo, A. Di Cicco, R. Parmar, R. Gunnella, S.J. Rezvani, Oxide coating role on the bulk structural stability of active $LiMn_2O_4$ cathodes, J. Phys. Chem. C 127 (18) (2023) 8649–8656.
[19] B. Gianfelici, F. Paparoni, R. Gunnella, S. Rezvani, N. Pinto, Adiabatic small polaron hopping in a-MoO_3 induced by oxygen vacancies, Mat. Sci. Semicond. Process. 201 (2026) 110073.
[20] F. Paparoni, A. Di Cicco, M. Minicucci, E. Mijit, S. Rezvani, A new cell for in situ high-temperature micro-Raman experiments: Studying the dynamics of oxygen vacancy formation in α-MoO_3, Phys. Chem. C 128 (2024) 15522–15532.
[21] M. Liebau, W. Suprun, M. Kasprick, R. Gläser, Transition metal oxides supported on TiO_2 as catalysts for the low-temperature selective catalytic reduction of NO_x by NH_3, Catalysts 15 (1) (2025).
[22] T. Jaouen, G. Jézéquel, G. Delhaye, B. Lépine, P. Turban, P. Schieffer, Work function shifts, schottky barrier height, and ionization potential determination of thin MgO films on Ag(001), Appl. Phys. Lett. 97 (23) 232104.
[23] L. Qiu, K. Chen, D. Yang, M. Zhang, X. Hao, W. Li, J. Zhang, W. Wang, Metal copper induced the phase transition of MoO_3 to MoO_2 thin films for the CdTe solar cells, Mater. Sci. Semicond. Process. 122 (2021) 105475.

[24] H. Lin, W. Xia, H.N. Wu, C.W. Tang, I. Irfan, Y. Gao, MoO_x as an efficient and stable back contact buffer for thin film CdTe solar cells, MRS Online Proc. Libr. 1447 (1) (2012) 45–52.
[25] F. Paparoni, E. Mijit, S. Kazim, M. Minicucci, N. Pinto, A. D'Elia, S. Macis, C. Kim, S. Huh, R. Gunnella, A. Marcelli, A. DiCicco, S.J. Rezvani, Metallic interface induced ionic redistribution within amorphous MoO_3 films, Adv. Mat. Interf. 9 (23) (2022) 2200453.
[26] M.T. Greiner, L. Chai, M.G. Helander, W.-M. Tang, Z.-H. Lu, Metal/metal-oxide interfaces: How metal contacts affect the work function and band structure of MoO_3, Adv. Funct. Mater. 23 (2) (2013) 215–226.
[27] E. Torretti, F. Paparoni, J. Cook, A. D'Elia, A. Di Cicco, L. Douillard, M. Faure, A. Marcelli, M. Minicucci, W. O'Neill, E. Rollin, M. Sparkes, B. Spataro, N. Lockwood, S. Rezvani, Interplay of deposition kinetics with metal diffusion in MoO_3-Cu heterojunctions, Appl. sur. Sci. 695 (2025) 162680.
[28] G. Landrot, E. Fonda, *Fastosh*: a software for the treatment of XAFS datasets of environmental relevance or acquired in *operando* conditions, J. Synchrotron Radiat. 32 (4) 1085–1094.
[29] A. Filipponi, A. Di Cicco, X-ray-absorption spectroscopy and n-body distribution functions in condensed matter. II. Data analysis and applications, Phys. Rev. B 52, 15135–15149.
[30] J. Baltrusaitis, B. Mendoza-Sanchez, V. Fernandez, R. Veenstra, N. Dukstiene, A. Roberts, N. Fairley, Generalized molybdenum oxide surface chemical state XPS determination via informed amorphous sample model, Appl. Surf. Sci. 326 (2015) 151–161.
[31] D.O. Scanlon, G.W. Watson, D.J. Payne, G.R. Atkinson, R.G. Egdell, D.S.L. Law, Theoretical and experimental study of the electronic structures of MoO_3 and MoO_2, J. Phys. Chem. C 114 (10) (2010) 4636–4645.
[32] K. Ajito, L. Nagahara, D. Tryk, K. Hashimoto, A. Fujishima, Study of the photochromic properties of amorphous MoO_3 films using Raman microscopy, J. Phys. Chem. B 99 (2002) 16383–16388.
[33] S.-H. Lee, M.-J. Seong, C. Tracy, A. Mascarenhas, J. Pitts, S. Deb, Raman spectroscopic studies of electrochromic a-MoO_3 thin films, Solid State Ion. 147 (2002) 129–133.
[34] M. Vasilopoulou, A.M. Douvas, D.G. Georgiadou, L.C. Palilis, S. Kennou, L. Sygellou, A. Soultati, I. Kostis, G. Papadimitropoulos, D. Davazoglou, P. Argitis, The influence of hydrogenation and oxygen vacancies on molybdenum oxides work function and gap states for application in organic optoelectronics, J. Am. Chem. Soc. 134 (39) (2012) 16178–16187.
[35] F.D. Hardcastle, I.E. Wachs, Determination of molybdenum–oxygen bond distances and bond orders by Raman spectroscopy, J. Raman Spectrosc. 21 (10) (1990) 683–691.
[36] A. Gaur, M. Stehle, K.V. Raun, J. Thrane, A.D. Jensen, J.-D. Grunwaldt, M. Høj, Structural dynamics of an iron molybdate catalyst under redox cycling conditions studied with in situ multi edge XAS and XRD, Phys. Chem. Chem. Phys. 22 (2020) 11713–11723.
[37] T. Ressler, O. Timpe, T. Neisius, J. Find, G. Mestl, M. Dieterle, R. Schlögl, Time-resolved XAS investigation of the reduction/oxidation of MoO_{3-x}, J. Catal. 191 (1) (2000) 75–85.
[38] F. Gunkel, D.V. Christensen, Y.Z. Chen, N. Pryds, Oxygen vacancies: The (in)visible friend of oxide electronics, Appl. Phys. Lett. 116 (12) 120505.
[39] G. Xiaoxi, W. Jiaheng, Z. He, M. Weiwei, J. Renhui, Z. Ligong, H. Tianlong, Z. Peili, J. Shuangfeng, W. Jianbo, Unexpected two-dimensional polarons induced by oxygen vacancies in layered structure MoO_{3-x}, J. Phys. Chem. Lett. 14 (2023) 11152–11159.
[40] H. Ding, H. Lin, B. Sadigh, F. Zhou, V. Ozoliņš, M. Asta, Computational investigation of electron small polarons in α-MoO_{3-x}, J. Phys. Chem. C 118 (29) (2014) 15565–15572.
[41] K. Inzani, M. Nematollahi, F. Vullum-Bruer, T. Grande, T.W. Reenaas, S.M. Selbach, Electronic properties of reduced molybdenum oxides, Phys. Chem. Chem. Phys. 19 (13) (2017) 9232–9245.
[42] R.S. Vemuri, K.K. Bharathi, S.K. Gullapalli, C.V. Ramana, Effect of structure and size on the electrical properties of nanocrystalline WO_3 films, ACS Appl. Mat. Interf. 2 (9) (2010) 2623–2628.
[43] B. Singh, B. Mehta, Relationship between nature of metal-oxide contacts and resistive switching properties of copper oxide thin film based devices, Thin Solid Films 569 (2014) 35–43.
[44] Y. Pan, X. Lu, T. Hui, C. Liu, B. Liu, W. Xu, C. Zhang, J. Sun, X. Qu, J. Zhang, High-temperature oxidation behaviour of TiAl alloys with Co addition, J. Mat. Sci. 56 (1) (2021) 815–827.
[45] M. Rellán-Piñeiro, N. López, One oxygen vacancy, two charge states: Characterization of reduced α-MoO_3(010) through theoretical methods, J. Phys. Chem. Lett. 9 (10) (2018) 2568–2573.
[46] L. Fan, X. Wang, F. Wang, Q. Zhang, L. Zhu, Q. Meng, B. Wang, Z. Zhang, C. Zou, Revealing the role of oxygen vacancies on the phase transition of VO_2 film from the optical-constant measurements, RSC Adv. 8 (2018) 19151–19156.
[47] R.C. Vincent, Y. Luo, J.L. Andrews, A. Zohar, Y. Zhou, Q. Yan, E.M. Mozur, M.B. Preefer, J.N. Weker, A.K. Cheetham, J. Luo, L. Pilon, B.C. Melot, B. Dunn, R. Seshadri, High-rate lithium cycling and structure evolution in Mo_4O_{11}, Chem. Mat. 34 (9) (2022) 4122–4133.
[48] M.S. da Luz, A. de Campos, B.D. White, J.J. Neumeier, Electrical resistivity, high-resolution thermal expansion, and heat capacity measurements of the charge-density wave compound γ-Mo_4O_{11}, Phys. Rev. B 79, 233106.
[49] S. Osman, C. Peng, F. Li, H. Chen, J. Shen, Z. Zhong, W. Huang, D. Xue, J. Liu, Defect-induced dense amorphous/crystalline heterophase enables high-rate and ultrastable sodium storage, Adv. Sci. 9 (36) (2022) 2205575.